High-speed terahertz reflection three-dimensional imaging for nondestructive evaluation

Kyong Hwan Jin,[1] Young-Gil Kim,[2] Seung Hyun Cho,[2] Jong Chul Ye,[1] and Dae-Su Yee[2,*]

[1]*Department of Bio and Brain Engineering, Korea Advanced Institute of Science and Technology, Daejeon 305-701, South Korea*

[2]*Center for Safety Measurements, Korea Research Institute of Standards and Science, Daejeon 305-340, South Korea*

[*]*dsyee@kriss.re.kr*

Abstract: We demonstrate high-speed terahertz (THz) reflection three-dimensional (3D) imaging based on electronically controlled optical sampling (ECOPS). ECOPS enables scanning of an axial range of 9 mm in free space at 1 kHz. It takes 80 s to scan a transverse range of 100 mm × 100 mm along a zigzag trajectory that consists of 200 lines using translation stages. To show applicability of the imaging system to nondestructive evaluation, a THz reflection 3D image of an artificially made sample is obtained, which is made of glass fiber reinforced polymer composite material and has defects such as delamination and inclusion, and is compared with an ultrasonic reflection 3D image of the sample.

OCIS codes: (110.6795) Terahertz imaging; (110.6960) Tomography; (120.4290) Nondestructive testing.

References and links

1. W. Withayachumnankul, G. M. Png, X. Yin, S. Atakaramians, I. Jones, H. Lin, B. Ung, J. Balakrishnan, B. W.-H. Ng, B. Ferguson, S. P. Mickan, B. M. Fischer, and D. Abbott, "T-ray sensing and imaging," Proc. IEEE **95**(8), 1528–1558 (2007).
2. C. Stoik, M. Bohn, and J. Blackshire, "Nondestructive evaluation of aircraft composites using reflective terahertz time domain spectroscopy," NDT Int. **43**(2), 106–115 (2010).
3. H. Zhong, J. Xu, X. Xie, T. Yuan, R. Reightler, E. Madaras, and X.-C. Zhang, "Nondestructive defect identification with terahertz time-of-flight tomography," IEEE Sens. J. **5**(2), 203–208 (2005).
4. Y. Morita, A. Dobroiu, K. Kawase, and C. Otani, "Terahertz technique for detection of microleaks in the seal of flexible plastic packages," Opt. Eng. **44**(1), 019001 (2005).
5. A. C. Kak and M. Slaney, *Principles of computerized tomographic imaging* (IEEE Press, New York, 1988).
6. B. Ferguson, S. Wang, D. Gray, D. Abbot, and X.-C. Zhang, "T-ray computed tomography," Opt. Lett. **27**(15), 1312–1314 (2002).
7. N. Sunaguchi, Y. Sasaki, N. Maikusa, M. Kawai, T. Yuasa, and C. Otani, "Depth-resolving THz imaging with tomosynthesis," Opt. Express **17**(12), 9558–9570 (2009).
8. E. Abraham, Y. Ohgi, M. A. Minami, M. Jewariya, M. Nagai, T. Araki, and T. Yasui, "Real-time line projection for fast terahertz spectral computed tomography," Opt. Lett. **36**(11), 2119–2121 (2011).
9. D. M. Mittleman, S. Hunsche, L. Boivin, and M. C. Nuss, "T-ray tomography," Opt. Lett. **22**(12), 904–906 (1997).
10. N. Karpowicz, H. Zhong, J. Xu, K.-I. Lin, J.-S. Hwang, and X.-C. Zhang, "Comparison between pulsed terahertz time-domain imaging and continuous wave terahertz imaging," Semicond. Sci. Technol. **20**(7), S293–S299 (2005).
11. V. P. Wallace, E. Macpherson, J. A. Zeitler, and C. Reid, "Three-dimensional imaging of optically opaque materials using nonionizing terahertz radiation," J. Opt. Soc. Am. A **25**(12), 3120–3133 (2008).
12. I. N. Duling, J. White, and S. Williamson, "High speed imaging with time domain terahertz," in 35th International Conference on Infrared Millimeter and Terahertz Waves (IRMMW-THz) (2010).
13. B. Schulkin and D. Brigada, J. St. James, T. Tongue, and X.-C. Zhang, "Progress toward handheld THz sensing," in 36th International Conference on Infrared, Millimeter and Terahertz Waves (IRMMW-THz) (2011).
14. T. Hochrein, R. Wilk, M. Mei, R. Holzwarth, N. Krumbholz, and M. Koch, "Optical sampling by laser cavity tuning," Opt. Express **18**(2), 1613–1617 (2010).
15. T. Yasui, E. Saneyoshi, and T. Araki, "Asynchronous optical sampling terahertz time-domain spectroscopy for ultrahigh spectral resolution and rapid data acquisition," Appl. Phys. Lett. **87**(6), 061101 (2005).

#171826 - $15.00 USD Received 5 Jul 2012; revised 20 Sep 2012; accepted 15 Oct 2012; published 25 Oct 2012

16. A. Bartels, A. Thoma, C. Janke, T. Dekorsy, A. Dreyhaupt, S. Winnerl, and M. Helm, "High-resolution THz spectrometer with kHz scan rates," Opt. Express **14**(1), 430–437 (2006).
17. Y. Kim and D.-S. Yee, "High-speed terahertz time-domain spectroscopy based on electronically controlled optical sampling," Opt. Lett. **35**(22), 3715–3717 (2010).
18. D. Stehr, C. M. Morris, C. Schmidt, and M. S. Sherwin, "High-performance fiber-laser-based terahertz spectrometer," Opt. Lett. **35**(22), 3799–3801 (2010).
19. J. Li and A. D. Heap, *A review of spatial interpolation methods for environmental scientists* (Geoscience, 2008).
20. F. Rutz, M. Koch, S. Khare, M. Moneke, H. Richter, and U. Ewert, "Terahertz quality control of polymeric products," Int. J. Infrared Millim. Waves **27**(4), 547–556 (2007).
21. L. S. Wilson and D. E. Robinson, "Ultrasonic measurement of small displacements and deformations of tissue," Ultrason. Imaging **4**(1), 71–82 (1982).
22. C. N. Liu, M. Fatemi, and R. C. Waag, "Digital processing for improvement of ultrasonic abdominal images," IEEE Trans. Med. Imaging **2**(2), 66–75 (1983).
23. D. P. Dandekar, C. A. Hall, L. C. Chhabildas, and W. D. Reinhart, "Shock response of a glass-fiber-reinforced polymer composite," Compos. Struct. **61**(1-2), 51–59 (2003).
24. C. Winnewisser, F. Lewen, and H. Helm, "Transmission characteristics of dichroic filters measured by THz time-domain spectroscopy," Appl. Phys., A Mater. Sci. Process. **66**(6), 593–598 (1998).
25. L. W. Schmerr, *Fundamentals of ultrasonic nondestructive evaluation: a modeling approach* (Springer, 1998).

1. Introduction

The transparency of nonconductive materials to terahertz (THz) radiation gives us chances to apply THz waves to characterize the internal structures of objects [1]. Such nondestructive evaluation (NDE) using THz waves was demonstrated for aircraft composites [2], defects in foam materials [3], and microleaks in plastic [4]. THz tomography can be used for NDE and there are two types of geometry for THz tomography: transmission and reflection [5]. In the transmission type, projection images should be obtained at various angles of projection [6–8]. In this case, attenuation of transmitted THz waves through an imaging target is measured and a tomographic image can be reconstructed using this attenuation information. A reconstruction algorithm is necessary to obtain a complete tomographic image. Therefore, the time for acquisition of projection images at various angles and image reconstruction is essential in the transmission tomography. In the reflection mode, tomographic images can be obtained from time-of-flight information [9]. Since the reflection mode needs neither rotation for projection angles nor image reconstruction, it is favorable for real-time B-scan (one-dimensional transverse scan along with axial scan) imaging or fast three-dimensional (3D) imaging.

The image acquisition time of THz reflection tomography is mainly determined by A-scan (axial scan) time. In the case of using a THz pulse, A-scans can be conducted through time delay scanning needed for measurement of THz waveforms. The use of a conventional mechanical delay line limits the A-scan rate to ~20 Hz [9–11]. Recently, a time delay scan rate was achieved up to several hundred Hz or 1 kHz by using mechanical delay tools specifically designed or optical sampling by cavity tuning [12–14]. Also, asynchronous optical sampling and electronically controlled optical sampling (ECOPS) were demonstrated for high-speed acquisition of THz waveforms [15–18]. Especially, ECOPS enabled us to acquire THz waveforms with a significant signal-to-noise ratio (SNR) at 1 kHz [17].

In this paper, we employ the ECOPS technique to demonstrate high-speed THz reflection 3D imaging. A-scan data are acquired at 1 kHz using ECOPS measurement of THz waveforms. The acquisition of A-scan data is combined with fast transverse moving of an imaging target by use of translation stages. The resulting imaging system enables us to acquire a 3D image of a sample with a transverse size of 100 × 100 mm^2 in 80 s. We also demonstrate applicability of the imaging system to NDE by comparing the THz and ultrasonic 3D images of a sample with internal defects.

2. High-speed THz reflection 3D imaging system

Our imaging system is illustrated in Fig. 1. Two femtosecond lasers synchronized at a repetition rate of 100 MHz are used for ECOPS measurement of THz waveforms. The time delay between optical pulses from the two lasers is controlled by an external offset voltage applied to the phase locked loop used for synchronization. The detailed description of our

#171826 - $15.00 USD Received 5 Jul 2012; revised 20 Sep 2012; accepted 15 Oct 2012; published 25 Oct 2012

ECOPS system can be found in [17]. Here, we set the time delay scan rate to 1 kHz using a triangular signal as the external offset voltage. A time delay window of 60 ps is obtained with a scan rate set to 1 kHz, in which the time delay varies linearly along with the real time. The time delay window of 60 ps allows us to scan an axial range of 9 mm in free space because the optical depth of an interface from the front surface of an imaging target equals to half the product of the time of flight inside the imaging target of a reflected pulse from the interface and the speed of light in vacuum. If the optical thickness of a sample is above 9 mm, a longer time delay window can be used at a lower scan rate [17]. We adopt a normal incidence configuration using a silicon beam splitter, where an imaging target is placed at the focal plane of a normally incident THz beam.

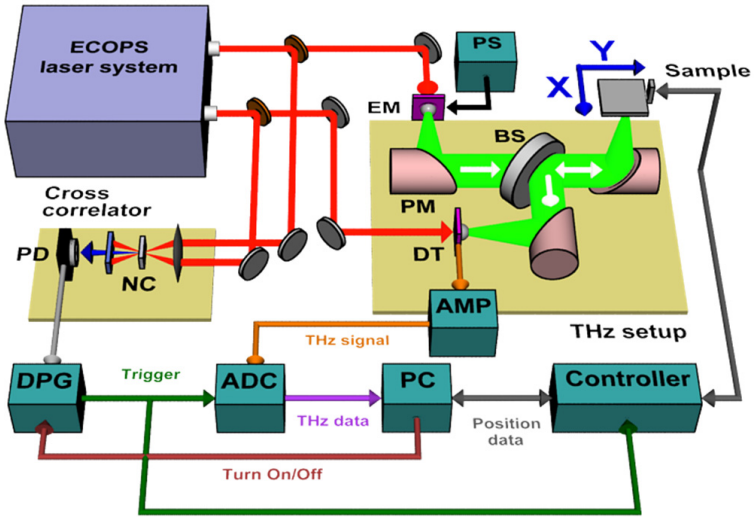

Fig. 1. Schematic diagram for our fast THz reflection 3D imaging system. EM: THz emitter, PS: power supply, PM: off-axis parabolic mirror, BS: silicon beam splitter, DT: THz detector, AMP: current amplifier, NC: nonlinear crystal, PD: photodetector, DPG: digital delay/pulse generator, ADC: analog-to-digital converter, PC: personal computer.

Certainly, the TTL signal of the function generator providing the triangular signal as the external offset voltage can be used to trigger a digitizer to acquire THz time-domain data. In order to reduce a timing jitter and vibration effects, however, we use a cross correlator to generate a trigger signal. The cross correlator produces two cross-correlation pulses within a 1 ms period because the time delay is scanned back and forth. We use a digital delay/pulse generator that starts to output a square pulse with a duration of 0.5 ms when triggered by a cross-correlation pulse. Then, the digital delay/pulse generator is triggered by only the leading pulse of two cross-correlation pulses less than 0.5 ms apart and resultantly outputs a 1 kHz TTL signal. THz time-domain data are acquired at 1 kHz by the digitizer triggered by the TTL signal and are used as A-scan data. The reference THz time-domain data of a mirror-reflected THz pulse has a SNR around 260. It is evaluated as the ratio of the peak amplitude to the standard deviation of noise in the time domain. Figure 2 shows examples of the cross-correlation signal, TTL signal, and THz time-domain data.

We transversely move an imaging target along a zigzag trajectory using translation stages. The total scan time depends on the transverse scan range. For a scan range of 100 mm × 100 mm, a total scan time of about 80 s can be obtained along a zigzag trajectory composed of 200 lines. Each line scan time is about 0.4 s at the maximum speed and acceleration of the translation stage and about 400 data points are recorded per line. During data acquisition, THz time-domain data have to be associated with their positions to form a 3D data cube (X, Y, T). Thus, it is necessary to obtain positions for each THz time-domain data point. Using trigger signals from the digital delay/pulse generator, we can simultaneously acquire positions as

#171826 - $15.00 USD Received 5 Jul 2012; revised 20 Sep 2012; accepted 15 Oct 2012; published 25 Oct 2012

well as THz time-domain data while translating an imaging target. This is because the TTL signal triggers the motion controller for the translation stages to start gathering positions at 1 kHz at the same time when the digitizer acquires THz time-domain data. The positions where THz time-domain data are acquired are not regular since the stage speed is not constant along the zigzag trajectory. Thus, we use the triangle-based linear interpolation to regrid the raw data into a regular 3D data cube [19].

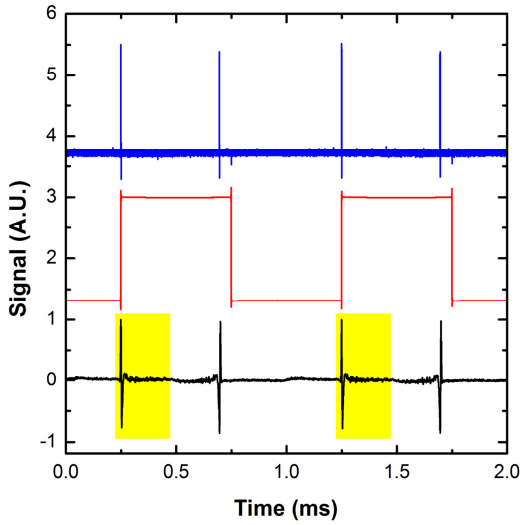

Fig. 2. Examples of the cross-correlation signal, TTL signal, and THz time-domain data. The blue line shows a cross-correlation signal that has two pulses within a 1 ms period. The digital delay/pulse generator outputs a 1 kHz TTL signal (red line), triggered by only the leading cross-correlation pulses. THz time-domain data (black line) are acquired by the digitizer triggered by the TTL signal. The parts of the THz time-domain data indicated by yellow color are used as A-scan data.

3. Its applications to NDE

We obtained THz 3D images of a floppy disk and an artificially made sample to demonstrate application of the imaging system to NDE. Figure 3(a) shows a two-dimensional (2D) image of the 3.5 inch floppy disk, constructed from the maximum values of A-scan data in a 3D data cube. We rendered a 3D volume of the floppy disk by using a rendering method which displays values around a noise level transparently and values around the maximum and minimum by opaque colors. The internal structure of the floppy disk, which consists of a plastic cover, a metal on the cover, a metal ring in the center, a magnetic storage medium, etc., is revealed clearly by the 3D tomographic image in Fig. 3(b). Basically, transverse resolution is determined by the spot size at the focal plane and axial resolution is proportional to the THz pulse width. In our experiments, the focal spot size and pulse width are estimated to be 2.3 mm and 2.1 ps, respectively.

Glass-fiber-reinforced polymer (GFRP) composite material is widely used for aircraft, railway, automobile, and wind turbine blades by virtue of the intensive tensile strength [20]. For a GFRP composite, quality control to find delamination or micro-cracking is important to prevent from critical failure of structures. For this reason, we applied our imaging system to NDE of a GFRP composite. We made a GFRP sample with artificial defects, as shown in the schematic design in Fig. 4. The sample dimensions are 100 mm, 100 mm, and 3 mm in width, length, and thickness. Internal defects like delaminations and inclusions were introduced into the sample. Eight rectangular delaminations with a nominal thickness of 0.2 mm are located around the edges, four of which lie at a depth of 1 mm and the others at a depth of 2 mm.

#171826 - $15.00 USD Received 5 Jul 2012; revised 20 Sep 2012; accepted 15 Oct 2012; published 25 Oct 2012

Also, four square pieces of Teflon with a nominal thickness of 0.025 mm are included around the center at a depth of 1.5 mm.

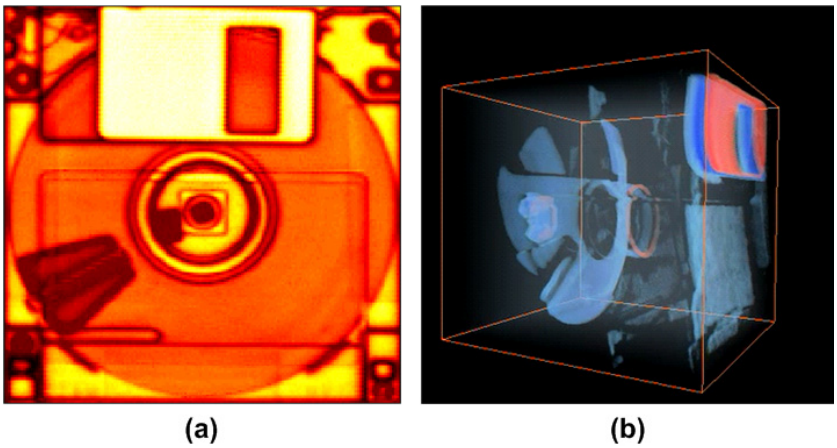

Fig. 3. (a) 2D and (b) 3D images of a floppy disk (Media 1), acquired using the THz imaging system.

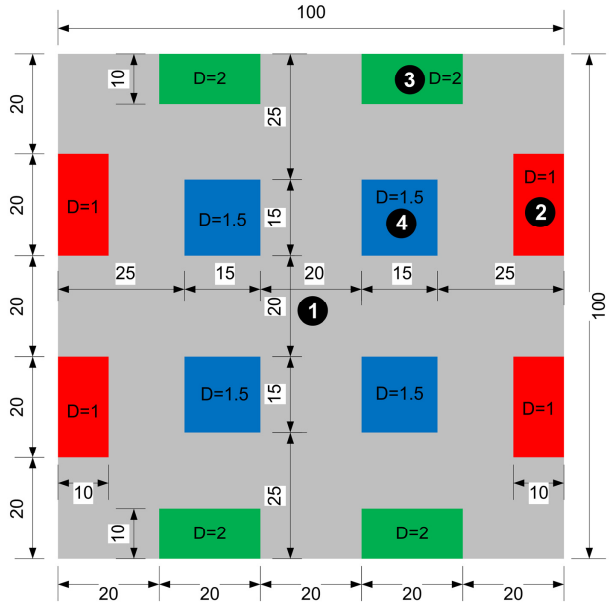

Fig. 4. Schematic design for the GFRP sample. The blue squares represent Teflon inclusions and the red and green rectangles delaminations. The depths where the defects lie are different, as indicated in the design. The unit of number is millimeter. The black-circled numbers indicate the regions where the A-scan data in Fig. 6 were acquired.

We obtained a 3D THz reflection tomographic image of the sample using our imaging system, as shown in Fig. 5(a). For comparison with ultrasonic tomography, which is one of the conventional methods for NDE, we also obtained ultrasonic images of the sample, as shown in Fig. 5(b) and 5(c). To acquire the ultrasonic images, an immersion C-scan test under water was conducted using a 10 MHz ultrasonic transducer. In contrast with the THz reflection tomography using a single-cycle pulse, additional processing of A-scan data is required for the ultrasonic reflection tomography due to a multi-cycle pulse. Figures 5(b) and

#171826 - $15.00 USD Received 5 Jul 2012; revised 20 Sep 2012; accepted 15 Oct 2012; published 25 Oct 2012

5(c) show the images obtained using the envelope function method through the Hilbert transform and the Wiener deconvolution method to process the A-scan data, respectively [21,22]. The eight delaminations are clearly visualized in the 3D THz image. Figure 5(b) shows the image with a relatively low axial resolution due to the restricted bandwidth of the ultrasound. In the ultrasonic image of Fig. 5(c), the lower delaminations are observed vaguely as smaller regions compared with the upper delaminations having the same size as the lower delaminations. In case of the inclusions, the ultrasonic image in Fig. 5(c) shows the structures better than the THz image.

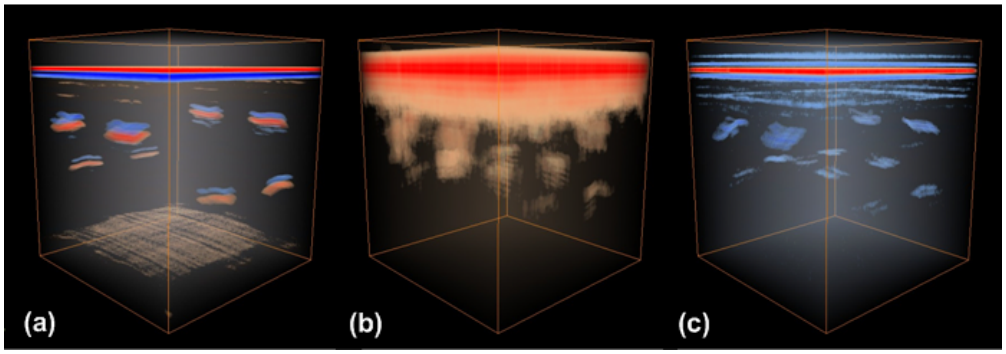

Fig. 5. (a) 3D THz image of the GFRP sample acquired using the imaging system (Media 2). (b) and (c) 3D ultrasonic images of the GFRP sample obtained from ultrasonic reflection tomography. The ultrasonic images in (b) and (c) were obtained using the envelope function (Media 3) and Wiener deconvolution (Media 4) methods to process the A-scan data, respectively.

We investigated the THz and ultrasonic A-scan data to understand the 3D images in more detail. Figure 6 shows A-scan data acquired at regions where there exist (1) no defect, (2) an upper delamination, (3) a lower delamination, and (4) a Teflon inclusion below, as indicated by the black-circled numbers in Fig. 4. Only the reflected pulses from the front and back surfaces are observed in region (1). The THz refractive index, ultrasonic wave speed, and THz and ultrasonic attenuation coefficients of the GFRP were extracted from the reflected pulses from the front and back surfaces in the A-scan data acquired at region (1). The THz refractive index of the GFRP was estimated to be 2.2 from the time delay between the reflected pulses from the front and back surfaces and the sample thickness [20]. The acoustic impedance of the GFRP was estimated to be 7.4×10^6 kg/m^{2}s using the measured ultrasonic wave speed of 3.7×10^3 m/s and the measured density of 2.0×10^3 kg/m^3, yielding similar values as given in ref [23]. In detail, the properties of GFRP composites depend on the production process and condition. The THz reflection coefficients between the GFRP and air and between the GFRP and Teflon were estimated to be 0.38 and 0.21, respectively, by using the THz refractive indices of the GFRP, air, and Teflon (1.44) [24] and the equation $r_{THz} = |n_1 - n_2| / |n_1 + n_2|$ where r_{THz} is the THz reflection coefficient between a medium 1 with a THz refractive index of n_1 and a medium 2 with a THz refractive index of n_2. The ultrasonic reflection coefficients between the GFRP and air and between the GFRP and Teflon were estimated to be 1 and 0.43, respectively, by using the acoustic impedances of the GFRP, air (4.1×10^2 kg/m^{2}s), and Teflon (2.97×10^6 kg/m^{2}s) [25] and the equation $r_{US} = |Z_1 - Z_2| / |Z_1 + Z_2|$ where r_{US} is the ultrasonic reflection coefficient between a medium 1 with an acoustic impedance of Z_1 and a medium 2 with an acoustic impedance of Z_2. Also, the THz and ultrasonic attenuation coefficients of the GFRP were roughly estimated to be 4.3 cm^{-1} and 7.5 cm^{-1}, respectively, from the peak-to-peak amplitude ratios between the reflected pulses from the front and back surfaces. From the attenuation coefficients, we can infer that the THz pulse is more advantageous than the ultrasonic pulse in imaging deep structures in GFRP composites.

#171826 - $15.00 USD Received 5 Jul 2012; revised 20 Sep 2012; accepted 15 Oct 2012; published 25 Oct 2012

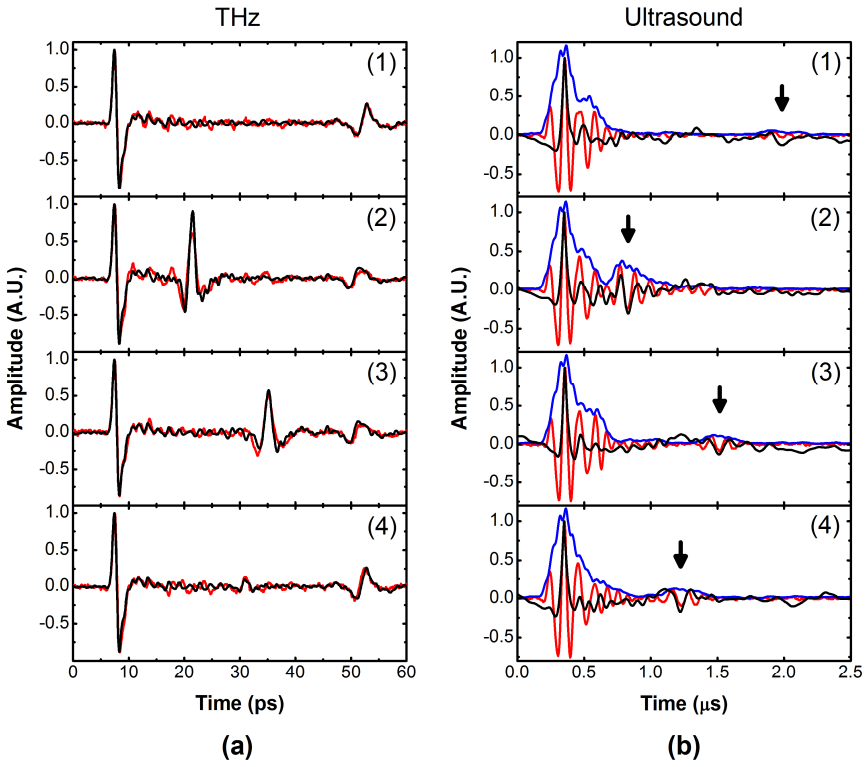

Fig. 6. (a) THz A-scan data (red line) acquired at the regions indicated by black-circled numbers in Fig. 4 and their simulation results (black line). (b) Ultrasonic A-scan data (red line) acquired at the same regions as in (a) and A-scan data obtained using the envelope function (blue line) and Wiener deconvolution (black line) methods. The reflected pulses from the back surface (1), the upper delamination (2), the lower delamination (3), and the inclusion (4) are indicated by arrows in (b). The vertical scale is normalized to the peak amplitude of the reflected pulse from the front surface.

We used the thickness, refractive index, and attenuation coefficient of the GFRP and the depths, thicknesses, and refractive indices of the defect layers to simulate the measured THz A-scan data as shown in Fig. 6(a). The simulation results were obtained by calculating the reflection of each of the frequency components of the reference THz pulse from the sample and then integrating all the reflected frequency components. Reflection from and transmission through the front surface, attenuation in the GFRP, Fabry-Perot (FP) reflection and transmission due to the defect layers, and reflection from the back surface were included in calculation of the reflection from the sample, since the defect layers act as FP etalons. On the whole, the simulation results are in good agreement with the measured data. In Fig. 6(b), the ultrasonic A-scan data obtained using the envelope function and Wiener deconvolution methods are shown along with the raw data.

The shape and amplitude of the reflected pulses from the defect layers are determined by transmission through the front surface, attenuation in the GFRP, and FP reflection from the defect layers. The reflected pulses from the delaminations are observed in region (2) and (3). The peak-to-peak amplitude ratio of the reflected pulse from the upper (lower) delamination to the reflected pulse from the front surface is measured to be about 0.57 (0.44) in the THz A-scan data and about 0.33 (0.12) in the ultrasonic A-scan data. The reflected pulses from the back surface behind the delaminations are shown in the THz A-scan data whereas they are not visible in the ultrasonic A-scan data due to no transmission through the delaminations. Also, the reflected pulses from the inclusions are observed in region (4). The resulting peak-to-peak amplitude ratio of the reflected pulse from the inclusion to the reflected pulse from the front

#171826 - $15.00 USD Received 5 Jul 2012; revised 20 Sep 2012; accepted 15 Oct 2012; published 25 Oct 2012

surface is measured to be around 0.12 in both the THz and ultrasonic A-scan data. Due to the higher noise level of the THz A-scan data than that of the ultrasonic A-scan data, the inclusion is more clearly seen in the ultrasonic 3D images than in the THz 3D image in Fig. 5.

In Fig. 6(a), the peak-to-peak amplitude of the reflected THz pulse from the inclusion is lower than even that from the lower delamination as well as that from the upper delamination. It indicates that the amplitude of the reflected THz pulse from the defects is more strongly dependent on FP reflection from the defect layers than attenuation in the GFRP. We calculated the FP reflection coefficients of the delaminations and inclusion using the equation

$$r_{FP}(\omega)=\left|-r+\frac{r\left(1-r^2\right)\exp(i\delta)}{1-r^2\exp(i\delta)}\right|=\sqrt{\frac{2r^2\left(1-\cos\delta\right)}{1-2r^2\cos\delta+r^4}}\quad\left(\delta=\frac{\omega}{c}2nd\right),\qquad(1)$$

where r is the reflection coefficient between the GFRP and defect, c is the speed of light in vacuum, and n and d are the refractive index and thickness of the defect layer, respectively. The refractive indices of the GFRP, air, and Teflon were approximated to be constant in the spectral range. The attenuation coefficient and thickness of the Teflon inclusion were so small that we ignored the attenuation terms. Figure 7 shows the amplitude spectra of the reflected THz pulses from the front surface and defects and the FP reflection coefficients of the defects. In comparison with the amplitude spectrum of the reflected THz pulse from the front surface, the high-frequency components of the amplitude spectra of the reflected THz pulses from the defects are greatly reduced due to the frequency-dependent attenuation in the GFRP. In addition, the FP effect of the defect layers results in the frequency-dependent FP reflection coefficients as shown in Fig. 7. The FP reflection coefficient of the inclusion is lower than that of the delamination in most of the spectral range. As a result, the amplitude of the reflected THz pulse from the inclusion is lower, as shown in Fig. 7. Therefore, we can see from Eq. (1) that it is difficult to find thin defects which satisfy the condition of *thickness* $\ll c/(4nf)$, where f is the peak-amplitude frequency.

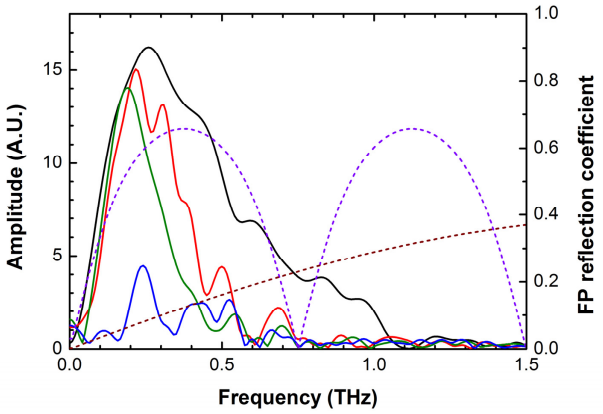

Fig. 7. The solid lines show the amplitude spectra of the reflected THz pulses from the front surface (black line), the upper (red line) and lower (green line) delaminations, and the inclusion (blue line). Also, the calculated FP reflection coefficients of the delamination and inclusion are indicated by the purple and brown dashed lines, respectively.

4. Conclusion

We have demonstrated fast THz reflection 3D imaging based on ECOPS measurement. The ECOPS measurement of THz waveforms enabled acquisition of A-scan data with a SNR as high as 260 at a rate of 1 kHz. For the range of 100 × 100 mm^2, transverse scan of 200 lines along a zigzag trajectory could be completed in 80 s using translation stages. The total scan time was limited to 80 s by the speed of the translation stages. Transverse scan can be

#171826 - $15.00 USD Received 5 Jul 2012; revised 20 Sep 2012; accepted 15 Oct 2012; published 25 Oct 2012

sufficiently fast by steering the THz beam instead of moving the imaging target and then the total scan time could be reduced to 40 s for 200 × 200 pixels at an A-scan rate of 1 kHz. Triangle-based linear interpolation was used for rendering 3D images from A-scan data acquired at irregular positions. The THz 3D images of a floppy disk and a GFRP sample with internal defects were obtained using the developed imaging system. By comparison of 3D THz and ultrasonic images, we showed the applicability of the high-speed THz reflection 3D imaging technology to NDE of a GFRP composite material. We found that THz tomography is more advantageous in imaging deep structures than ultrasonic tomography due to lower attenuation. THz tomography could show even defects behind delaminations in contrast to ultrasonic tomography. Also, it turned out that the amplitude of a reflected THz pulse from a defect layer is greatly affected by the layer thickness due to the FP effect and that it is difficult to discover a thin defect whose optical thickness is much smaller than a fourth of the wavelength corresponding to the peak-amplitude frequency.

Acknowledgment

This work was supported in part by Ministry of Education, Science, and Technology through the project KRISS-11011029 and in part by National Research Foundation of Korea - Grant funded by the Korean Government (NRF-2012-M2A2A9-2012035659).

#171826 - $15.00 USD Received 5 Jul 2012; revised 20 Sep 2012; accepted 15 Oct 2012; published 25 Oct 2012